ARTICLE IN PRESS

Optics and Lasers in Engineering xxx (xxxx) xxx

Contents lists available at ScienceDirect

Optics and Lasers in Engineering

journal homepage: www.elsevier.com/locate/optlaseng

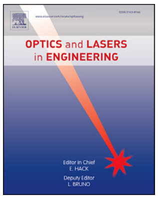

Process zone morphology and melt dynamics in laser remote fusion cutting (RFC) revealed by high-speed X-ray imaging

Silvana Burger [a,b,*], Carola Forster [a,b], Christoph Spurk [c], Marc Hummel [c],
Alexander Olowinsky [d], Felix Beckmann [e], Julian Moosmann [e], Michael Schmidt [a,b]

[a] *Friedrich-Alexander-University Erlangen-Nuremberg, Institute of Photonic Technologies, Erlangen, 91052, Germany*
[b] *School of Advanced Optical Technologies (SAOT), Friedrich-Alexander-University Erlangen-Nuremberg, Erlangen, 91052, Germany*
[c] *RWTH Aachen University, Chair for Laser Technology LLT, Aachen, 52074, Germany*
[d] *Fraunhofer-Institute for Laser Technology ILT, Aachen, 52074, Germany*
[e] *Institute of Materials Physics, Helmholtz-Zentrum Hereon, Geesthacht, 21502, Germany*

ARTICLE INFO

Keywords:
Laser material processing
Laser beam cutting
X-ray imaging
Synchrotron radiation
Melt dynamics

ABSTRACT

Laser material processing procedures yield numerous benefits, as non-contact manipulation of the workpiece, high precision, and extensive automation capabilities. For metal joining, laser beam welding is a widely used process employed in industry, for example in automotive body construction and in the production of electronic components. With the same optical setups as usually used for laser beam welding, a melt ejection can be induced in sheet metal, resulting in the formation of a cut. This enables laser remote fusion cutting (RFC) based on a melt ejection without the need for tools near the process zone. A comprehensive understanding of the conditions and mechanisms causing the melt ejection or preventing it is yet to be achieved.

In this study, in-situ observations of the process zone in RFC were performed using high-speed X-ray imaging with synchrotron radiation, achieving frame rates up to 18 kHz for steel samples and 28 kHz for AlMg3 samples. Key features of the process zone morphology are extracted by means of image processing from the recordings, such as the angle of front wall inclination or the ejection direction for different process parameters. The front wall angle for RFC is in line with an established model for the front wall angle in laser beam welding. Propagation-based phase-contrast imaging reveals the melt film at the cutting front, showing a decrease of the melt film thickness with increasing feed velocities. Melt dynamics at transitions between process states of cutting and not cutting could be observed. The temporal resolution was insufficient to capture humps in the melt film at the front wall in steel samples. These were resolved for AlMg3 samples, confirming that humps at the front wall play an important role in the melt dynamics.

1. Introduction

Laser material processing offers non-contact processing, high precision and excellent conditions for automation. Laser beam welding and laser beam cutting of metals are two established processes in industry. In conventional laser beam fusion cutting, the metal is molten as a result of the irradiation with the laser beam and the material ejection is achieved through a gas stream applied through a nozzle. For this purpose, the gas nozzle must be positioned directly above the process zone and elaborate system technology is required. The positioning of the nozzle and the workpiece regarding exact standoff distance of the nozzle is essential for a high-quality cut [1].

Studies like [2] and [3], demonstrate that conventionally utilized laser beam sources and optics from laser beam welding can also be used to induce a melt ejection from the process zone and generate cuts in metal. A schematic overview of the process zone is given in Fig. 1. The melt is ejected by the pressures building in the process zone, a gas stream applied via a nozzle is not necessary. This method is referred to as laser beam remote cutting (RFC) in literature [4]. Remote processing allows manipulation from a distance, eliminating the need for a tool near the process zone. This enables a change between remote laser beam welding and cutting solely through parameter adjustments.

However, in RFC unstable melt ejections can occur, resulting in discontinuous cuts [5]. At the current state of research, the exact melt dynamics in RFC are not clear and the mechanisms defining the parameter window of RFC are not known.

---

* Corresponding author.
E-mail address: silvana.burger@fau.de (S. Burger).

https://doi.org/10.1016/j.optlaseng.2024.108756
Received 2 September 2024; Received in revised form 20 November 2024; Accepted 5 December 2024

Please cite this article as: Silvana Burger et al., *Optics and Lasers in Engineering*, https://doi.org/10.1016/j.optlaseng.2024.108756

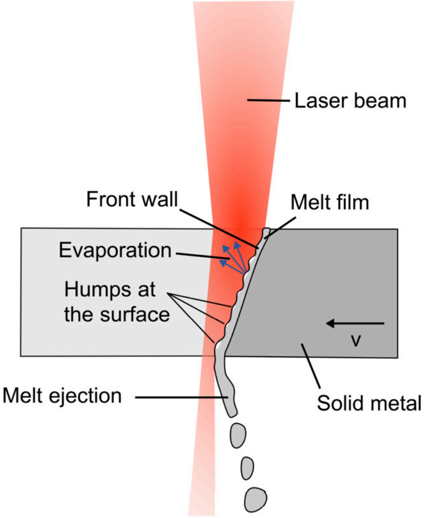

Fig. 1. Process zone in laser beam remote fusion cutting (RFC).

To acquire a deeper understanding of these mechanisms, further insights into the behaviour of the process zone are important. For analytical process models or simulations, the quantification of essential properties of the process zone such as the cutting front inclination, the melt film at the cutting front and the melt ejection angle are of importance.

The experimental investigations reported in literature give insights regarding features of the process zone morphology, but a detailed observation is difficult due to the limited accessibility for process observation. An estimation of the cutting front inclination angle from high-speed images is reported in [6]. The front wall angles from high-speed recordings give a good estimation of the angle, but the form of the front wall, which can for certain parameters exhibit a bend, cannot be taken into account with this method. A dependence of the melt ejection angle on the feed velocity was observed in [3]. To explain the mechanisms leading to the observed angle, further investigations are needed, utilizing advanced process observation methods and additional experiments not only varying the feed velocity but also the laser power.

The exact forces acting on the melt in RFC and driving the melt ejection are not well understood. Detailed high-speed imaging of the keyhole front in laser keyhole welding was conducted in [7], where for certain parameter combinations RFC was observed. In the recordings bright spots travelling down the keyhole front wall are visible, which are interpreted as areas of increased temperature. This observation provides an explanation of the driving mechanism of the downward melt expulsion [7]: A wavy surface forms at the keyhole front (as depicted in Fig. 1), resulting in locally varying inclination angles of the surface. This leads to areas with increased absorption of the laser radiation and consequently higher temperatures. This could lead to locally increased evaporation and an increase in the recoil pressure on the surface caused by evaporation. The humps at the surface lead to an acceleration of the melt towards the bottom of the metal sheet. Many aspects of this theory need further investigations, like the manifestation and size of the melt humps at the front wall and their movement. The increase in absorption at humps at the front wall was analytically modelled in [8], with the angle dependent absorption described by the fresnel law. The absorption at the humps is particularly relevant for the wavelength of 1 µm which is nowadays commonly used in industrial welding and cutting [8].

Conventional laser beam fusion cutting and laser beam keyhole welding share the principle of laser material interaction and similarities regarding the process zone with RFC. In laser beam fusion cutting insufficient melt ejections can for example be attributed to insufficient melting or to boundary layer separation of the gas stream from the nozzle diminishing momentum transfer to the melt [9]. Bright spots at the front wall have also been observed for conventional fusion cutting [10], which might be related to melt humps and might influence burr formation. The 3D measurements in [11] support this hypothesis of bright spots being related to humps at the surface in case of conventional fusion cutting. As in conventional fusion cutting the melt is accelerated by a gas jet, the results cannot be directly transferred to RFC. However, also in conventional fusion cutting, high laser powers influence the melt flow through evaporation phenomena [12]. Laser beam keyhole welding is based on the same mechanisms as RFC, with the melt flowing around a capillary and creating a joint instead of being pushed out of the process zone. There are existing models, for example regarding the front wall inclination of the process zone [13], which could also apply for RFC. This needs to be experimentally investigated, as the conditions in RFC differ from keyhole welding, for example the rear keyhole wall is not present in RFC, instead there the cutting kerf forms. Pirecing at the begin of cutting and welding is similar to RFC, keyhole formation has been observed in [14] and modelled in [15]. This needs further investigations for the case of RFC, where full penetration of the sample is needed, and the dynamics of the melt stream leaving the process zone are of importance. Keyhole stability in welding is studied in [16], where it is pointed out that deformations of the keyhole can lead to multiple reflections and unsuitable energy incoupling into the meltpool, leading to evaporations and blowholes. In [17] irregular weld seams are attributed to energy input in the melt pool as well. It is to be investigated if similar effects of altered energy incoupling cause instabilities in RFC.

More extensive observations of the melt dynamics in RFC with high temporal resolution could be helpful for explaining instabilities of the cutting process. Such observations are challenging as the events in the process zone occur on a small spacial and temporal scale. The accessibility of the process zone for high-speed imaging is limited to a top view and to the melt ejection. In order to generate insights from a side view, investigations with a glass setup were conducted [18], where thermal shock resistant glass acts as a replacement edge of the process zone. This allows for a side view of the wavy surface of the process zone. On the downside the glass wall can influence the process zone and the melt ejection behaviour, as it influences the absorption of the laser beam in the process zone, the heat conduction and the melt dynamics. Furthermore, the glass wall on one side of the process zone induces an asymmetry to the process zone.
X-ray imaging can be conducted without these direct influences on the process zone, however the temporal resolution is limited when conventional X-ray tubes are used, due to the high density of the metal samples. The reported frame rates of high-speed imaging with X-ray tubes are around 1 kHz [19] for aluminium samples. Imaging with synchrotron radiation offers higher framerates and better image quality. The X-ray radiation generated at a synchroton facility, is characterized by high photon energies and a high photon flux [20]. It has successfully been applied for imaging the process zone in conventional laser beam fusion cutting [21], in keyhole welding [22] and in laser based additive manufacturing [23].

This study aims to address the missing information regarding the morphology of the process zone in RFC. To achieve this, high-speed X-ray imaging with synchrotron radiation of the process zone in RFC is conducted. Specifically, the study aims at imaging features of the morphology of the process zone which could explaining the melt ejection, like the inclination of the front wall, the position and extent of the melt ejection at the bottom of the process zone. Theoretical considerations from the literature suggest, that the downward acceleration of the melt is significantly influenced by the melt film at the front wall and its surface topography [8], however experimental investigation is challenging. Therefore, this study examines the thickness of the melt film and the occurrence and size of humps along the front wall. In literature, instabilities in keyhole welding have been attributed to certain keyhole geometries [16]. As this might be similar in RFC, it is analyzed if states with melt ejection and without melt ejection display visible differences in morphology.

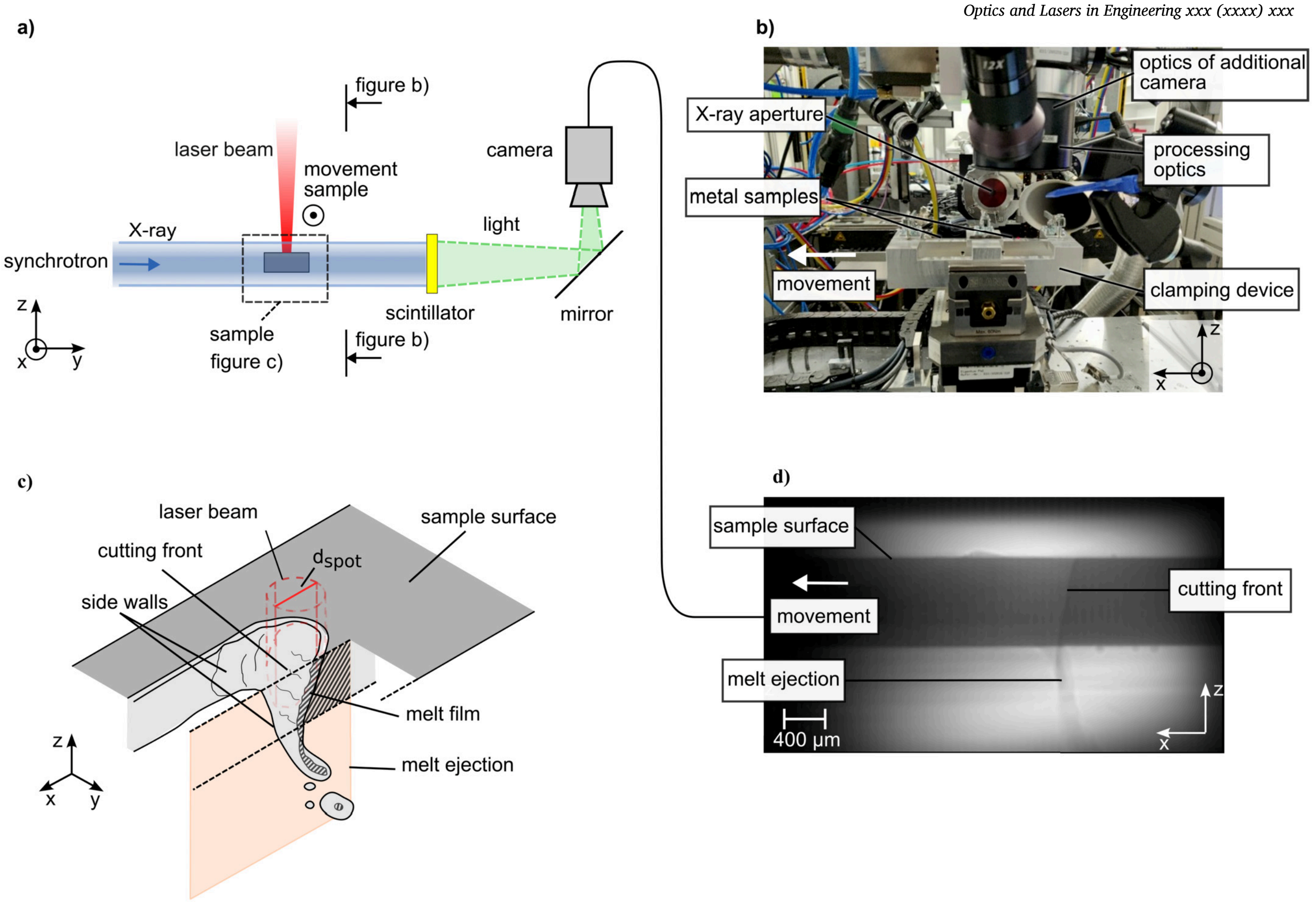

Fig. 2. Setup for high-speed X-ray imaging of RFC. a) Schematic overview. b) Setup with the clamping device on the axis system. c) Process zone during RFC with cutting front, melt ejection and the cutting kerf. d) High-speed X-ray image of the process zone in RFC.

2. Methods

In this study, high speed X-ray imaging of the process zone of laser material processing is conducted. In the experiments, a metal sample is moved on an axis system and processed with laser light. The process zone is imaged with synchrotron radiation, as shown in Fig. 2.

2.1. *Laser material processing experiments*

In the experiments, DC04 steel samples are processed with infrared laser radiation. The laser parameters are listed in Table 1. The laser light source is the YB:YAG disk laser TruDisk6001 (Trumpf GmbH, Ditzingen, Germany). Processing was conducted in focal position with a 400 µm diameter laser spot. The laser light is guided through a 400 µm dual core fiber (BrightLine Weld, Trumpf) consisting of an inner fiber with 200 µm diameter and an outer ring fiber of 400 µm diameter. The fiber end is imaged onto the sample by the processing optics with a magnification ratio of 1:1. By coupling in 6 % of the laser power in the inner fiber, and the other 94 % in the outer fiber, a 400 µm top hat beam profile is approximated. (This function was unlocked by the manufacturer. In the conventional setup the minimum ratio in the inner fiber is 10 %.) The resulting profile was measured with the beam caustic measurement device MicroSpotMonitor (Primes GmbH, Pfungstadt, Germany). It shows a top hat profile with a small peak of elevated intensity in the middle of the spot.

The clamping of the samples can be seen in Fig. 2 b, together with the high-speed axis system for movement (Jenny Science AG, Rain, Switzerland) and the exit point of the X-ray radiation at the setup. The samples are sized 80 mm x 2 mm x 0.8 mm (or 1 mm) in x, y, and z direction. For simplifying the workflow at the X-ray setup with its safety perimeters for radiation protection, the clamping device can hold two samples.

In the experiments, the clamping device is moved by the axis system with feed velocity v_{feed} and the laser beam with laser power P is acti-

Table 1
Laser system.

Parameter	Value
Maximum Power	6 kW
Wavelength (λ)	1030 nm
Fiber Type	Dual Core
Fiber Diameter	400 µm
Spot Size	400 µm
Rayleigh length	2.4 mm
Beam Profile	Top Hat
Intensity distribution	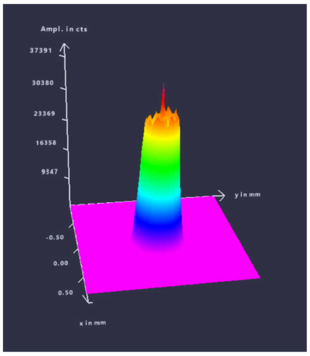

vated when the sample passes the processing position, creating a cut or weld of 30 mm length.

The study focuses on cutting of steel samples (DC04). Processing the samples with 4 kW is investigated for feed velocities between 50 mm s^{-1} and 210 mm s^{-1}. For medium feed velocities, where stable cutting is achieved at 4 kW, cutting at two lower laser powers of 3 kW and 2 kW is also investigated. From [18] it is known that the humps at the front wall move with high speed. As prior to the study it was unclear whether the setup could achieve exposure times short enough to observe humps on the front wall accurately, for comparison a small set of AlMg3 samples is observed. The low density of aluminium enables high quality recordings at short exposure times.

2.2. High-speed X-ray imaging setup

For imaging, high energy X-ray radiation is generated at the synchrotron facility DESY (Deutsches Elektronen-Synchrotron). When the electron beam in the storage ring PETRA III passes through sections equipped with undulator magnets, so called synchrotron radiation, which is high energy X-ray radiation, is emitted. The radiation passes a monochromator and is deflected to the beamline where the experiments are conducted.

The experiments in this study were conducted at beamline P07- High Energy Material Science Beamline, which is operated by Helmholtz Center Hereon and DESY. Imaging was conducted at photon energies of 74 keV for the steel samples and 37 keV for the aluminium samples.

The X-ray beam (cross-section: 2 mm x 2 mm) first interacts with the metal sample and afterwards with a scintillator material. When excited by the X-ray radiation the scintillator emits light in the visible regime. This light can be captured by the sensor of the high-speed camera (i-SPEED 727, iX Cameras). In the present study the scintillator material GAGG(Ce) was used, emitting at a wavelengh of 520 nm. With this setup the varying attenuation of the X-ray beam when passing through the geometry of the process zone is recorded and an absorption image is obtained.

In the process zone of RFC or laser keyhole welding, different phases of solid metal, liquid metal and vapour/ambient gas are present. As there is only a small difference in density between solid and liquid metal in the experiments, solid and liquid phase display a very similar absorptivity of the X-rays making it difficult to distinguish between solid and fluid in the data of absorption images. However, there is a stronger difference in the effect on the phase of the X-rays when passing through either solid or fluid metal. This can be used to differentiate between solid and liquid by applying phase contrast imaging methods. [20]

In the experiments, the absorption images were complemented with the free propagation based phase contrast imaging. With this method, edges between solid and liquid in the sample are enhanced, as an abrupt change in phase leads to an interference pattern with Fresnel fringes [20]. In order to apply this technique, the sample must be thin and the scintillator has to be placed at a suitable distance from the sample to allow for free propagation, which were 3.5 m for the described setup.

The videos were recorded experimenting with different frame rates and exposure times. In order to image the highly dynamic process zone, short exposure times are required. The limiting factor is the low amount of light captured by the camera sensor during short exposure times. For imaging of the DC04 steel samples frame rates between 7.5 kHz and 30 kHz have been tried, with the corresponding maximum exposure times between 133 μs and 33.3 μs. The few experiments at the highest framerate are very noisy, and require massive post processing, so this work focuses on framerates up to 18 kHz. For the AlMg3 samples imaging at frame rates between 18 kHz and 45 kHz has been performed, with the corresponding maximum exposure times between 55.6 μs and 22.2 μs.

2.3. Image processing for data evaluation

In the raw images a general view of the process zone can be observed, however fine details are not visible. The raw images are flat field corrected and normalized to account for the inhomogeneous illumination by the X-ray beam and for enhancing visibility in the darker area of the metal sample. Therefore, each image is divided by the mean of 120 images of the metal sample in the beginning of the video before the laser is turned on. Afterwards, the resulting images are rescaled to the whole range of grey values. The image processing algorithms are implemented in Python, for visualization purposes, the software ImageJ is utilized. This procedure leads to a shift of the gray values of the resulting images: The gray values in the processed image do not directly indicate the transmission, but the transmission relative to the pure sample before material processing starts. Furthermore, this procedure can lead to artefacts when the sample position in z-direction slightly changes during the recording, resulting in dark or bright lines at the bottom or the top of the sample.

From the image data different properties of the process zone are extracted, as

- the inclination angle of the cutting front,
- the thickness of the melt film at the cutting front,
- the angle of the melt expulsion at the bottom of the process zone.

2.3.1. Measurement of the inclination angle of the front wall

The angle of the cutting front wall is automatically determined using image processing algorithms. For each image of the recording, the sample position and the position of the cutting front are detected. Therefore, the Canny Edge Detection algorithm and the Line Hough Transform algorithm from the scikit-image package [24] are applied. The image processing procedure is shown in Fig. 3: For extraction of the cutting front inclination angle, the original recorded images are used without flat field correction, in order to avoid the above mentioned artefacts of the corrected images.

The image is downscaled by factor 2 and the Canny Edge detection algorithm is applied, the resulting image is dilated, increasing the line thickness. The steps of downscaling and dilation enhance the detectability of lines in the Line Hough Transform if there are slight deviations from perfectly straight lines. Then the Line Hough Transform is applied. Peaks in the Hough transformed image correspond to lines in the original image. After two strong peaks corresponding to the horizontal lines are identified, for the front wall inclination only the area of the Hough image corresponding to the area between the detected lines is considered. In the Hough Transformed image, a peak corresponding to the cutting front wall is searched, with the condition, that the front wall inclination should lie in the range between 90° and 30°, corresponding to 0° and 60° in the Hough image (Fig. 3 c).

The resulting front inclinations are filtered in order to exclude misdetections, meaning that non-physical abrupt changes of the measured value of more than 5° between two frames in a video are excluded. Afterwards the mean cutting front angle and its standard deviation for different parameters are extracted. The precision of the front wall angle measurement is high, due to the clear imaging contrast of the front wall. Potential minor sources of uncertainty are such as slight variations in the exact pixel locations designated as the wall's edge in the edge detection step. Such deviations, however, have a minimal impact on the overall accuracy due to the relatively small pixel size in the downscaled image when compared to the total length of the front wall. To quantify the impact of pixel-level deviations on the angle measurement, consider typical front wall angles of approximately 75°. In this context, a displacement of the endpoints of the front wall of two pixels (10 μm) in the downscaled image would, due to the relatively flat slope of the $\arctan$ function in this area, result in a variation of only 1° in the measured angle.

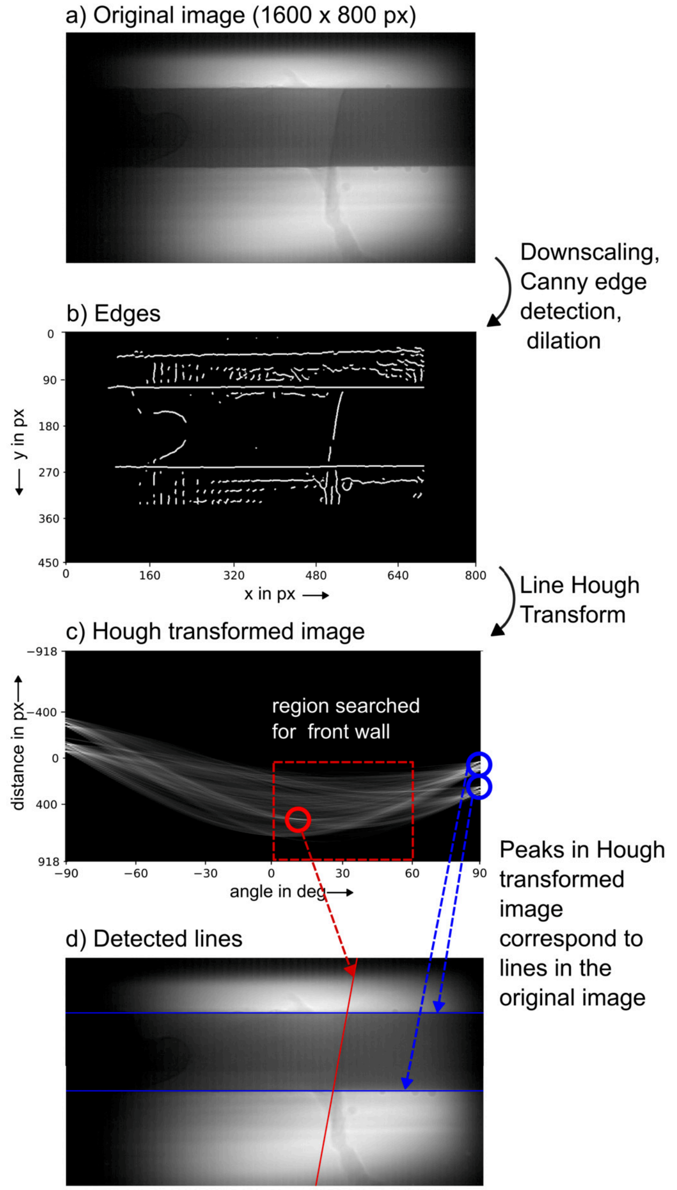

Fig. 3. Extraction of the front angle through application of the Hough Transform. Downscaling, Canny edge detection and dilation are applied to the original image (a, b). Downscaling and dilation increases detectability of lines that are not perfectly straight. The resulting image is Line Hough transformed (c). Peaks in the Hough Transformed image correspond to lines in the original image (d). The front wall angle lies between 30° and 90° (corresponding to 0° and 60° in the Hough Image) and is extracted from the red area in c. This procedure is applied to each frame in the video.

2.3.2. *Measurement of the melt film thickness at the front wall*

Furthermore, the melt film thickness at the keyhole front is investigated in the recordings. With the imaging setup for free propagation based phase contrast, differentiation between solid and liquid phase should be possible. For the AlMg3 samples a dark line dividing melt and solid is directly visible. For the DC04 steel samples, this signal is weak and more difficult to extract. There is increased image noise coming with the high absorption of the steel samples and the short illumination times. In order to be able to extract the position of the Fresnel fringe of the solid-liquid interface at the cutting front wall, processing is done as shown in Fig. 4: In a range of the recording where the front wall is in a stable state, the mean image of 20 images is calculated, reducing the noise in the image. The mean image is then smoothed with the Savitzky-Golay filter. The Savitzky-Golay filter fits a low order polynomial to a subset of adjacent datapoints. The advantage of the Savitzky-Golay filter compared to alternative smoothing methods, like moving average, is that minima and maxima are contained [25]. The filtered images are analyzed with ImageJ, where the gray values along a line perpendicular to the cutting front are plotted. There, after the first local minimum corresponding to the vapour-liquid interface, a second local minimum is visible corresponding to the liquid-solid interface. The measurement of fringe distances in this study is subject to several sources of uncertainty, primarily due to the finite pixel resolution of the detector and potential variations in fringe thickness influenced by small movements and propagation effects. One camera pixel corresponds to 2.5 μm in reality, which sets the basic spatial resolution limit. The clarity of fringe positions is estimated to be within ±2 px, leading to an inherent positional uncertainty of ±5 μm for each fringe. When measuring the distance between two fringes, this positional uncertainty can compound, resulting in a maximum difference of ±4 px. This corresponds to a total uncertainty of ±10 μm in the measurement of the fringe spacing.

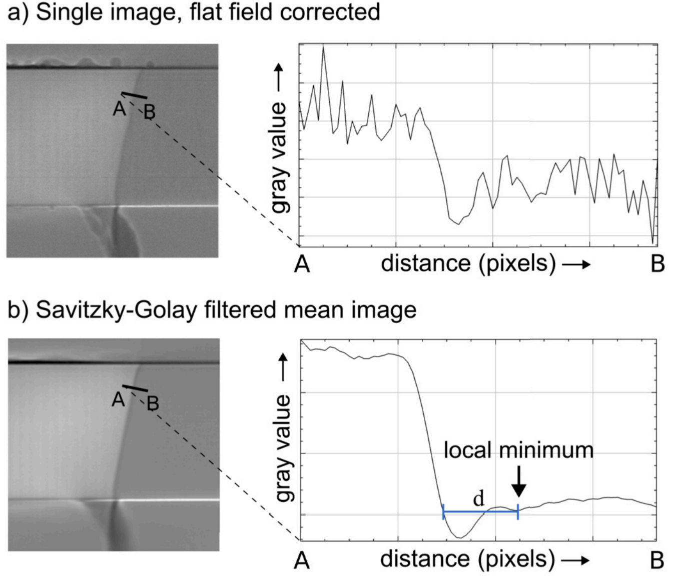

Fig. 4. Measurement of the melt film thickness at the front wall: a) The images of the steel samples are noisy due to the low transmission of X-rays in combination with short exposure times. A clear position of the fresnel fringe corresponding to the fluid-solid interface cannot be determined from the noisy image. b) Calculating the mean image of 20 images and applying the Savitzky-Golay filter increases the visibility of the second dark line in the images and allows for measurement of the distance *d* between the gas-fluid interface and the fluid-solid interface.

2.3.3. *Measurement of the ejection angle of the melt stream*

For the automated evaluation of the melt ejection angle, a line is fitted to the melt stream. This fitting is performed on mean images created from sets of 20 individual images. These mean images effectively display the direction of the melt ejection without the gaps caused by individual droplets. The resulting angle is measured in the bottom 20 % of the images in the recordings. This is implemented with the peak-finding function of the scipy python package which is applied on the gray values of horizontal lines in the images, the procedure is shown in 5. The inclination of a line fit through the peak positions gives the angle of the ejected melt stream. In practice, the measurement of the melt ejection angle is potentially subject to error. For example the measurement is not exactly done in the same distance from the sample if the sample exhibits a slight bend. Such deformations can occur as a result of sample preparation or for parameters with high heat input into the sample.

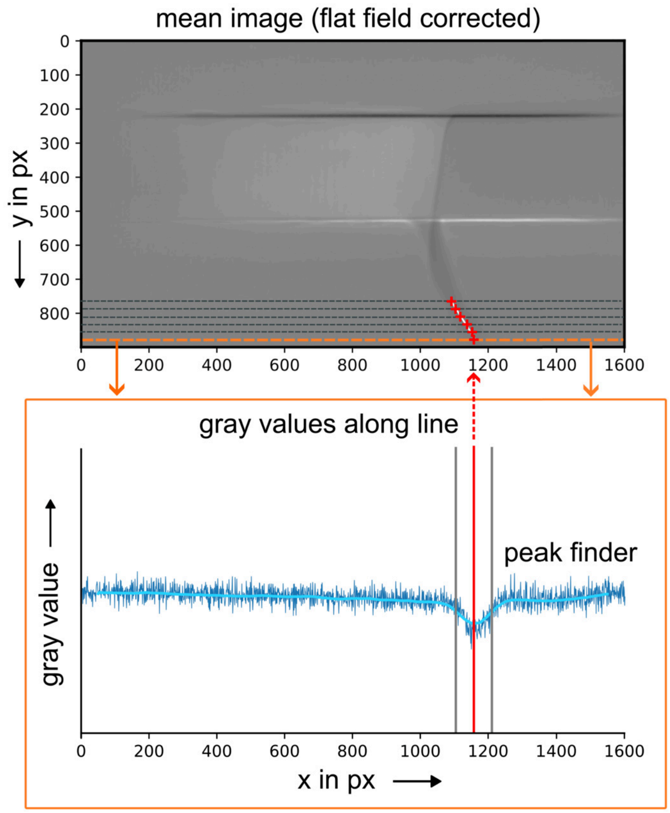

Fig. 5. Image processing for automated measurement of the melt ejection angle. The gray values along lines in the bottom area of the images are plotted, the signal is smoothed and peak finding is applied. A line is fit through the peak positions (marked in red). The line inclination gives the inclination angle of the ejected melt stream.

3. Results and discussion

3.1. General observations and morphology of the process zone

The typical process zone in RFC for DC04 steel (Fig. 6 a) displays the cutting front and the melt flow from the bottom of the process zone. Edges of the sample that result in an abrupt change in the phase of the X-ray radiation are enhanced with the free propagation based phase contrast imaging technique [20]. This results in clearly visible edges at the bottom and the top of the metal sample, as well as a darker line at the border between fluid and gas in the process zone. This imaging technique is used to reveal the interface between solid material and melt film at the cutting front. For the steel samples this line is very faint and often not directly distinguishable within the image noise. For AlMg3 samples (Fig. 6b), this line at the cutting front is directly visible in the recordings. For AlMg3 a thicker melt film forms, which behaves highly dynamic. For the investigated parameters, in AlMg3 a continuous melt flow out of the process zone does not form, but detaching spatter. The detachment of spatter for the AlMg3 samples is typically downward directed and tilted in feed direction. In contrast, the typical direction of melt expulsion for the DC04 steel is downward and tilted against feed direction. The amount and small size of the spatters implies, that the formation of the cut in AlMg3 occurs due to a combination of evaporation of the material, detachment of spatter, and movement of the remaining material to the sides of the cutting kerf.

In the X-ray images, the overall side profile of the cutting front is visible, for DC04 displaying a generally straight line with a curvature at the top for most parameters.

The occurrence of small moving melt humps at the front of the process zone is expected, as postulated in [7] and explained in the introduction. These humps are not visible in the recordings due to their small size and rapid movement in combination with the frame rates and exposure times that are possible with the setup for the steel samples. At high frame rates of 18 kHz slight deviations from the cutting front line are visible, but the exact contour and movement of melt humps cannot be resolved.

In the experiments the formation of partial or continuous cuts could be observed for most parameters of the investigated parameter window. Typical cutting results are shown in Fig. 7. Some of the resulting bridges at both sides of the kerf exhibit a noticeable gap as in Fig. 7 a. This is due to the heat input in the samples. When the hot melt is not expelled from the process zone, for example at defects or during welding, the heat input in the sample is increased and sample deformation can occur (Fig. 7 c). Continuous cuts where most of the melt is expelled exhibit only minimal deformation (Fig. 7 b).

The recordings demonstrate the existence of distinct process zone morphologies in response to varying feed velocities: In the case of low feed velocities (Fig. 8 a) the front wall is steep. For high feed velocities (Fig. 8 b) the front wall is more tilted.

At low feed velocities, the majority of the melt expulsion occurs at the uppermost front of the process zone. In contrast, at high feed velocities, a broader melt expulsion via the side walls is observed.

Furthermore, a melt expulsion at the top of the metal sample without detachment is present for high feed velocities. This results in an increased surface roughness of the sample.

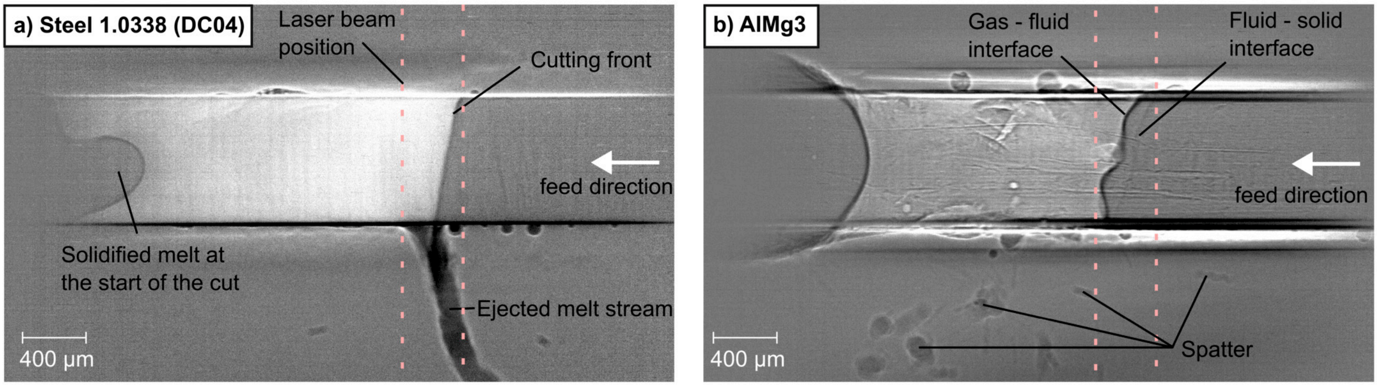

Fig. 6. High-speed X-ray images of the process zone during RFC. a) The cutting front and the ejected melt stream are clearly visible for DC04 steel ($P_{laser} = 4\,\mathrm{kW}, v_{feed} = 130\,\mathrm{mm\,s^{-1}}$). b) For AlMg3 only a small amount of melt is expelled in form of spatter. At the front of the process zone, the fresnel fringe at the interface of solid and liquid metal is visible ($P_{laser} = 3\,\mathrm{kW}, v_{feed} = 130\,\mathrm{mm\,s^{-1}}$).

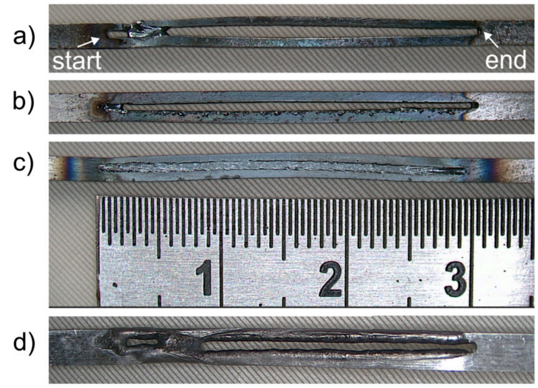

Fig. 7. Examples of processed samples: a) Cut with defect 2 mm after the start (steel, $v_{feed} = 110\,\mathrm{mm\,s^{-1}}$, $P_{laser} = 4\,\mathrm{kW}$). b) Cut with melt remaining at the start (steel, $v_{feed} = 190\,\mathrm{mm\,s^{-1}}$, $P_{laser} = 4\,\mathrm{kW}$). c) Full penetration weld, no RFC (steel, $v_{feed} = 130\,\mathrm{mm\,s^{-1}}$, $P_{laser} = 2\,\mathrm{kW}$). d) Cut in AlMg3 ($v_{feed} = 130\,\mathrm{mm\,s^{-1}}$, $P_{laser} = 3\,\mathrm{kW}$).

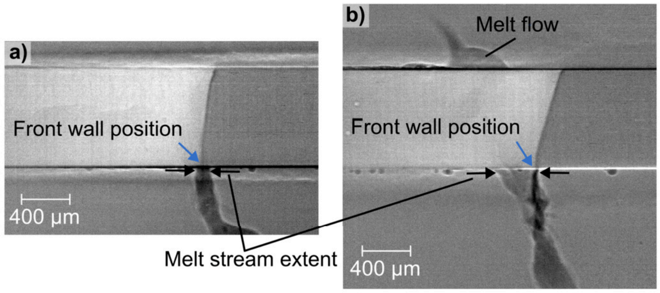

Fig. 8. Process zone for different v_{feed}. a) $v_{feed} = 90\,\mathrm{mm\,s^{-1}}$, $P_{laser} = 4\,\mathrm{kW}$: Steep cutting front. The melt expulsion occurs at the uppermost front of the process zone. b) $v_{feed} = 190\,\mathrm{mm\,s^{-1}}$, $P_{laser} = 4\,\mathrm{kW}$: For higher v_{feed} the cutting front is more tilted and the melt expulsion occurs not only at the uppermost front of the process zone, but in a larger area at the keyhole front. Additionally, a melt flow to the top of the metal sheet is present.

3.2. The piercing process

An exemplary piercing process at the begin of a cut is shown in Fig. 9. The first mark of the laser beam on the metal sample (a) is of the diameter 400 µm, as the spot size of the laser beam. The exact position of the laser beam on the sample is extracted from the image of this first visible impact. The keyhole is deepened (b) and the slight intensity peak in the middle of the beam profile (as shown in Table 1) becomes visible in the keyhole morphology. When the keyhole reaches the bottom of the metal sample (c), melt is ejected in the form of fast spatter. This first melt ejection is directed downwards and slightly against feed direction. More melt is ejected from the process zone in a broader jet with slower velocities than the previous spatter (d). A melt bulge forms at the back wall of the process zone. The melt is slightly pushed upwards by the evaporation from the cutting front (d, e). When the process zone advances from the start of the cut, surface tension causes the remaining melt to assume a rounded shape (f) which solidifies. The melt ejection angle typically decreases once piercing is complete and the melt ejection stabilizes.

From the experiments the time required to create a keyhole and fully pierce through the samples are extracted. From this the “drilling speed” $v_d = d_{sample}/\Delta t$ is calculated. The resulting drilling speeds are shown in Table 2. When measuring the time from the first appearance of an interaction of the laser beam with the metal to the complete piercing, the temporal quantization error is of the order of one frame, resulting in the errors of the drilling speed given in the table. The errors depend on the framerates f, which have been altered between experiments in order to optimize imaging. The error is calculated as $Temporal\ Quantization\ Error = \frac{d_{sample}}{(N+1)\cdot T} - \frac{d_{sample}}{N\cdot T}$ with the time T between frames $T = 1/f$ and the number of frames N between first interaction of the laser beam with the sample and complete piercing. The drilling velocities can be used for modelling the front wall inclination as shown in the following section.

Table 2
Drilling velocity.

Laser power P in kW	Feed velocity v in mm/s	Drilling velocity in mm/s	Measurement error of the drilling velocity in mm/s (temporal quantization error of one camera frame)
4	130	640	45
3	130	533	24
2	130	320	11

3.3. Process zone morphology during cutting

3.3.1. Angle of the cutting front

From the X-ray recordings, the exact measurement of the inclination angle α of the cutting front is possible. The inclination angle α is decreasing for increasing feed velocities, similarly as in keyhole welding. The exact behaviour is shown in Fig. 10 a. Examples of the corresponding process zone are depicted in Fig. 11.

The behaviour is in line with the theoretical model of the front wall inclination for the related process of laser keyhole welding described by Fabbro et al. in [13]. In Fig. 10 a the theoretical curves for the front angles based on the measured drilling velocities (Table 2) with equation (1) are shown as dotted lines. In [13] the front angle is modelled as a function of the welding speed (feed velocity) and the ‘drilling speed’ v_d. The drilling speed determines the rate at which material is displaced and depends on the absorbed intensity and thermal properties of the material. During the characteristic time interval Δt as the laser spot of size d_{spot} transverses a point on the sample, drilling occurs at a velocity of v_d. This leads to:

$$\tan\alpha = \frac{v_{feed}}{v_d} \tag{1}$$

with α as depicted in Fig. 10. The curves show good agreement with the experimentally measured values of the front angle.

There might be a deviation of the *measured* drilling velocity from the drilling velocity *during cutting*, as the measurement is conducted at the begin of the cut. At the begin of the process, the surrounding material is not yet heated, which can result in a lower drilling velocity compared to cutting. On the other hand, as the keyhole forms, with the backwall present more energy can be coupled in through multiple reflections than during cutting, thereby potentially increasing the measured drilling velocity. For the experiments with $P_{laser} = 3\,\mathrm{kW}$ there is a slight deviation of the measured angles from theory curve based on the drilling velocity. The drilling velocity during piercing might be higher than during cutting here. The front angle of different experiments at the same parameters are well aligned, leading to partially overlapping datapoints. In RFC there is no rear wall of the process zone like in keyhole welding, reducing energy input by multiple reflections of the laser radiation. However, the results show that, despite this difference, the inclination angle of the cutting front aligns with the theoretical curve for keyhole welding.

3.3.2. Melt film thickness at the cutting front

Although for steel samples the melt film at the cutting front is not directly visible in most single images in the recordings, the signal of the Fresnel fringes can by enhanced by post processing, as described in section 2.3. The measured melt film thicknesses at the front wall are shown in Fig. 10 b. For increasing feed velocities the melt film thickness decreases.

As for feed velocities over $v_{feed} = 150\,\mathrm{mm\,s^{-1}}$ the melt films become

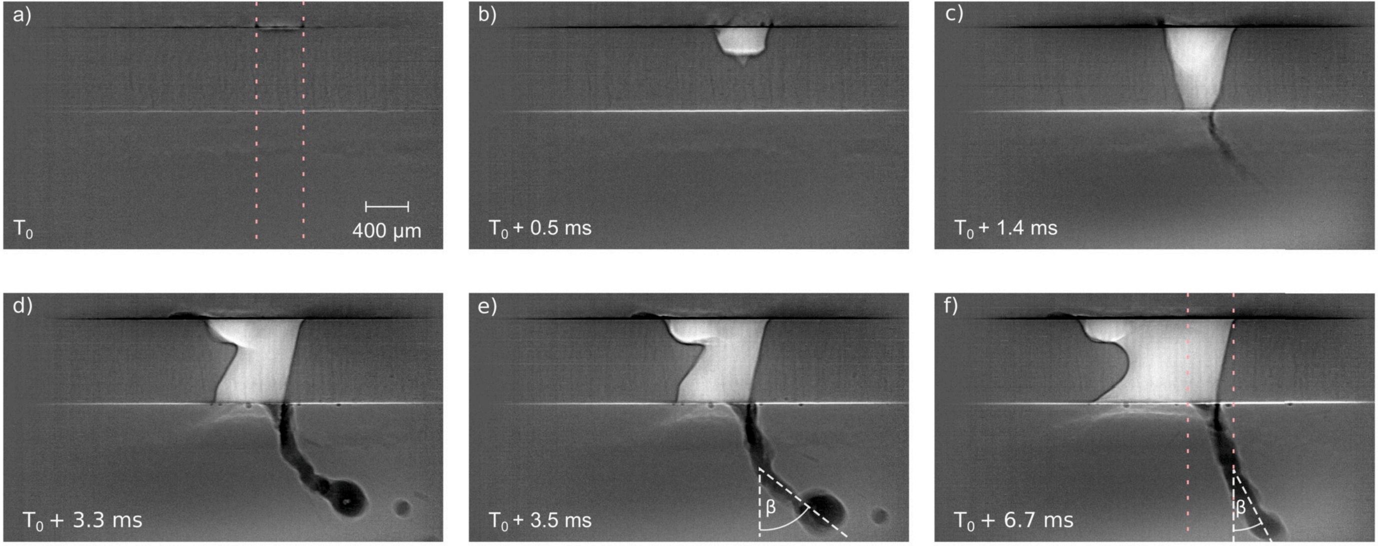

Fig. 9. Piercing process for $v_{feed} = 150\,\mathrm{mm\,s^{-1}}$, $P_{laser} = 4\,\mathrm{kW}$, recorded at a frame rate of 10000 fps. The exact position of the laser beam on the sample is extracted from the beginning of the piercing process (a, b) Melt expulsion against feed direction starts directly when the laser beam fully penetrates the sample (c). At the start the melt ejection is often tilted towards the sample (d, e), which can in some cases lead to melt adhesion and defects. When the process stabilizes, the melt is ejected downwards (f).

very thin, resulting in distances around 10 px an smaller in the images, the fresnel fringes are not clearly distinguishable and are not evaluated. In case of RFC, the melt film thickness appears to correspond to the width of the melt expulsion at the leading edge of the process zone's bottom.

From the theoretical perspective, the melt film thickness is influenced by the thermal diffusivity of the material and the duration of the interaction with the laser beam, which is determined by the feed velocity and the spot size, and by the pressure acting on the melt film. As for higher feed velocities the duration of interaction with the laser beam decreases, the observed decrease of the melt film thickness with the feed velocity is expected.

The experiments with different laser powers lead to similar melt film thicknesses. The two experiments with the lowest laser power of $P_{laser} = 2\,\mathrm{kW}$ (where no cutting occurs) show slightly higher melt film thicknesses than the experiments with the same feed velocities at higher laser powers. This could be explained by the lower recoil pressure acting on the melt at the front wall for $P_{laser} = 2\,\mathrm{kW}$.

For $P_{laser} = 4\,\mathrm{kW}$, $v_{feed} = 50\,\mathrm{mm\,s^{-1}}$ the melt film thickness is not evaluated, as the process zone is instable. An enlarged molten area at the front can be observed, that seems to be caused by the thermal influence of the melt accumulation at the bottom of the sample. This is described more detailed in section 3.4, where instable behaviour of the process zone is discussed.

The melt film thickness in combination with the position and extent of the melt stream, which is also parameter dependent (see Fig. 8), establishes a foundation for theoretical modelling of the flow from the process zone and the parameter window of RFC. Process zones with high melt film thicknesses at lower feed velocities are more easily be deformed by pressure changes and might be more susceptible to instabilities. In contrast, the downward material transport that enables RFC may be compromised for very thin melt film thicknesses at high feed velocities.

3.3.3. Angle of the melt ejection

The melt ejection angles for the experiments are depicted in Fig. 12. The values are extracted from the bottom area of the recordings, as described in section 2. In Fig. 12, the following trends can be observed:

As the feed velocity increases, the angle of melt ejection approaches a vertical ejection. A similar dependence of the ejection angle on the feed velocity has previously been reported in [3].

Experiments at reduced laser power ($P_{\mathrm{laser}} = 3\,\mathrm{kW}$) show increased melt ejection angles.

For the experiments with increased sample thickness of 1 mm, the mean melt ejection angle is decreased and the standard deviation is high. During the first few recordings, imaging at the beamline was adjusted ‘on the fly’ and only a small area beneath the sample was imaged, so these ejection angles (at $v_{feed} = 90\,\mathrm{mm\,s^{-1}}$ and part of the experiments at $v_{feed} = 110\,\mathrm{mm\,s^{-1}}$) are not included in the evaluation.

The effects that cause the melt stream to bend below the process zone are not fully understood. In theory, the ejection angle is influenced by a number of factors, including the process zone geometry, the momentum of the ejected melt, the redirection of the melt stream below the process zone by the recoil pressure, adhesion forces, air friction due to the movement of the sample relative to the ambient and an observed angle due to the relative movement of the sample to the camera.

One important factor driving the melt ejection is the recoil pressure due to evaporation. In the process zone the melt is pushed to the solid walls of the process zone by the recoil pressure. At the bottom of the process zone the solid material balancing the recoil pressure ends, so a redirection of the melt stream by the recoil pressure is possible. However, the melt stream is less bent for higher laser powers (Fig. 11A and 11B), meaning that the redirection by recoil pressure can only be part of the explanation of the melt direction in combination with other phenomena.

The dependence of the melt ejection angle on the laser power could be explained by different melt velocities and therefore momentum in z-direction. If the melt flow in z-direction is slower for lower laser powers, forces in x- or y-direction at the bottom of the process zone (like induced by the recoil pressure or cohesive forces) have a stronger influence on the ejection direction.

The dependence of the melt ejection angle on the feed velocity could be explained partly by the relative movement of the frame of reference of the sample to the frame of reference of the camera. However, for melt ejection velocities around $1\,\mathrm{m/s}$ or $2\,\mathrm{m/s}$ it can easily be estimated that this effect should not induce a change the angle of more than about 5° between $v_{feed} = 50\,\mathrm{mm\,s^{-1}}$ and $v_{feed} = 200\,\mathrm{mm\,s^{-1}}$.

The decrease of the ejection angle with the feed velocities could be caused by higher melt velocities in z-direction. Higher feed velocities could lead to higher melt velocities and a higher momentum of the melt in z-direction, so that redirecting forces at the bottom of the process zone have a smaller impact on the ejection direction.

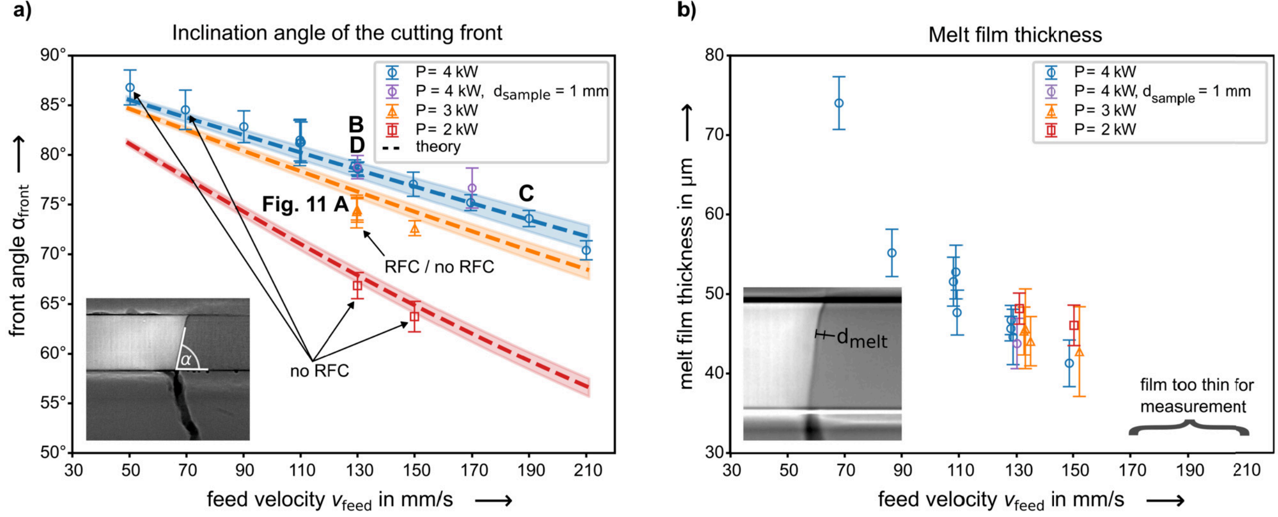

Fig. 10. a) Inclination angle of the front wall for different laser powers P_{laser} and feed velocities v_{feed} ($d_{spot} = 400\,\mu$m). Each point represents mean and standard deviation of the angles extracted from the frames one whole video of a 3 mm cut or weld (N>300). The curves represent the theoretical course from equation (1) for the measured drilling speeds. The coloured corridors show the theoretical course for the measurement uncertainty of the drilling speeds. b) Melt film thickness at the cutting front wall, extracted from the Fresnel fringes in the X-ray images after Savitzky-Golay filtering with mean value and standard deviation, N = 10.

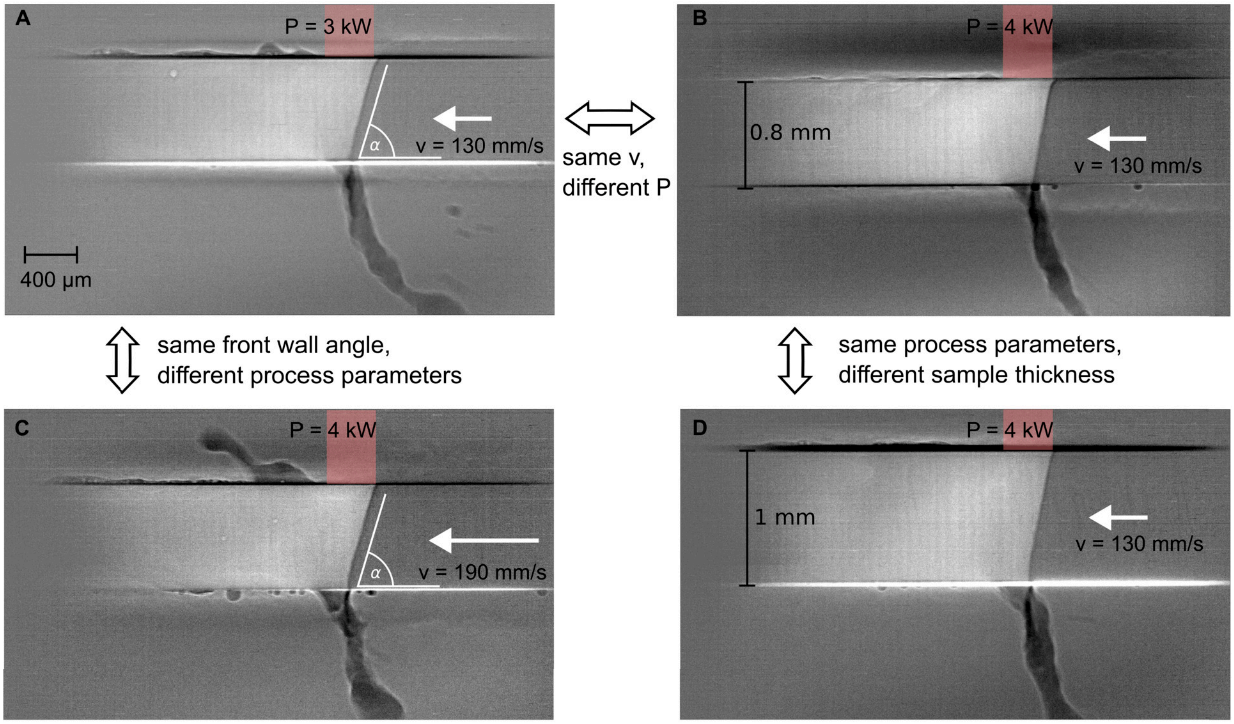

Fig. 11. For the investigated parameter range, higher laser powers (see A vs. B) and higher feed velocities (see A vs. C) lead to a more vertical directed melt ejection. A and C display the same inclination of the cutting front, but a different direction of melt ejection, which shows that the melt ejection angle is not determined by the front wall angle. The high feed velocity in C leads to a pronounced upward melt ejection at the top of the sample which is constantly present. The thicker sample of 1 mm in D displays a more vertical melt ejection than the 0.8 mm thick sample in B.

The process zone morphology and the position and extent of the melt stream (Fig. 8) seem to be important factors for the ejection of the melt stream. For higher feed velocities a higher amount of the ejected melt flows along the side walls of the process zone. For the steel samples cohesive forces as the surface tension are acting on the melt in such a way, that it tends to leave the sample in a melt stream (not as individual droplets). The ejection angle results from the combination the melt streams from side walls of the process zone and from the tip of the cutting front. Liquid jets emanating from a non-circular-symmetric aperture can result in complex behaviour, like chain oscillations investigated in [26]. There the oscillations are generated by pouring liquid from a non-circular orifice. The oscillation is caused by the asymmetry in combination with cohesive forces and inertia. Further formations which are caused by the collision of two laminar jets are described in [27]. These investigations of the process zone of RFC at DESY show that the melt ejection in RFC is even more complex, with melt moving at different velocities at the tip of the cutting front and at the side walls, joining in one stream and recoil pressure acting on the melt stream.

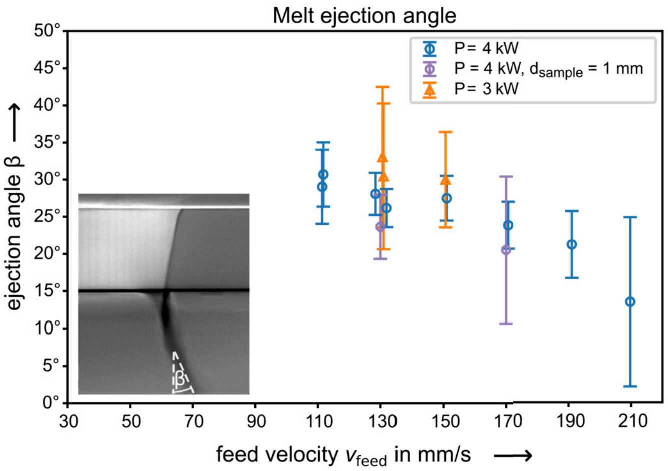

Fig. 12. Measured angle of the melt ejection, mean value and standard deviation, N>100. For increasing feed velocity the ejection angle decreases. The experiments with the reduced laser power of 3 kW lead to a higher ejection angle. The experiments with increased sample thickness lead to a lower ejection angle. The highest feed velocity shows a high standard deviation due to a widely spread melt ejection with varying centroid and fluctuations of the ejection direction.

Fig. 12, as well as the images in Fig. 11 a and c demonstrate, that the front inclination angle does not directly determine the melt ejection angle: Higher feed velocities lead to lower front inclination angles α in combination with a lower melt ejection angle β. Lower laser powers lead to lower front inclination angles in combination with higher melt ejection angles β.

For the investigated thicker samples the mean ejection angles are smaller (Fig. 12 and Fig. 11 B vs. D). As the melt film thickness at the front wall is similar for both thicknesses (Fig. 10 b), there could be a higher amount of melt flowing along the side walls before being ejected, influencing the ejection direction. To deeper evaluate the processes determining the direction of the melt ejection, additional investigations, for example with tracer particles giving detailed insights into the melt movements, could be beneficial.

3.3.4. Melt ejection at the top of the sample

For low feed velocities the upward ejection is not present. For higher feed velocities a melt ejection at the top of the sample is present (see Fig. 8). The position of the melt ejection is behind the laser beam position. For the experiments at $P_{laser} = 4\,\mathrm{kW}$ very small top-melt ejections start at $v_{feed} = 130\,\mathrm{mm\,s^{-1}}$ (Fig. 11 B) and the amount of melt increases for increasing feed velocities. For high feed velocities of $v_{feed} = 190\,\mathrm{mm\,s^{-1}}$ (Fig. 11 C) and above there is a constant upward directed melt stream forming a melt bulge. For the experiments at $P_{laser} = 2\,\mathrm{kW}$ and 3 kW a top-melt ejection is present and its amount is increased compared to the higher laser power experiment at the same feed velocity (for example see Fig. 11 A vs. B).

The underlying mechanisms influencing the top-melt ejection at surface are not clear. A possible explanation is the melt movement induced by shear forces from the vapour jet streaming off the front wall. As for all the experiments where a top melt ejection was observed, the front wall angle is below 80 degree (Fig. 10 a), the vapour jet from the front wall might be a possible explanation, but the observation could also be related to other hydrodynamic effects. This needs further investigation. The constant and strong top-ejection for high feed velocities of $v_{feed} = 190\,\mathrm{mm\,s^{-1}}$ could be caused by a higher amount of backstreaming melt or higher dynamics at higher feed velocities. Furthermore, for high feed velocities the cutting front is more tilted and the vapour jets are directed upwards.

Part of the melt remains at the surface of the material and solidifies there, leading to an increased roughness at the metal surface. The rest of the melt flows back into the cutting kerf and solidifies at the side walls of the cutting kerf.

3.4. Observations regarding the melt dynamics in the process zone

From the X-ray recordings of the experiments, not only can information about the process zone geometry be extracted, but the melt dynamics can also be observed with high temporal resolution. Of particular interest are the melt dynamics that may be related to the discontinuous cuts mentioned in the introduction. In the following, a period of stable RFC is defined as a period of steady melt ejection from the process zone leading to an uninterrupted cut. The discussion will address instabilities and changes in process zone morphology, such as the closure of the cut due to melt flowing back into the kerf.

3.4.1. Melt accumulation after piercing at the start of a cut

One typical instability of RFC in this study is the accumulation of melt at the bottom of the metal sheet shortly after piercing the sample. This can be observed for the lower feed velocities up to $130\,\mathrm{mm\,s^{-1}}$ and is shown in Fig. 13. After piercing, melt flows out of the process zone, but does not detach from the sample (Fig. 13 a, b). The bulk melt

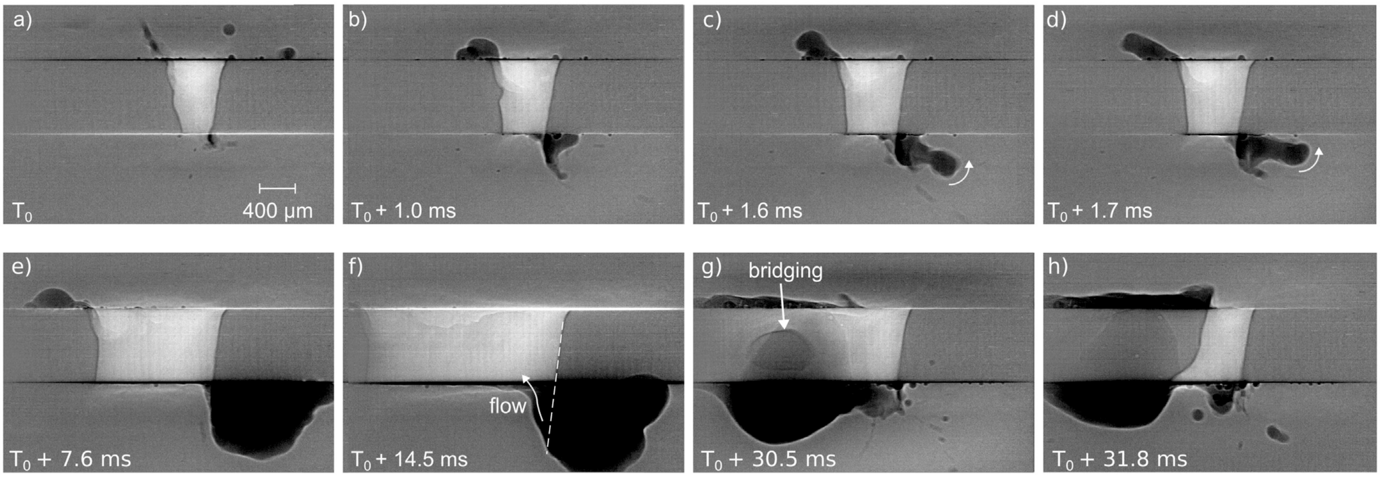

Fig. 13. Melt accumulation on the bottom of the metal sample building during piercing and closing the cut at $v_{feed} = 110\,\mathrm{mm\,s^{-1}}$, $P_{laser} = 4\,\mathrm{kW}$. a, b) Piercing and instant melt attachment. c, d) Melt is pushed out of the process zone, but a movement toward of the bottom of the process zone sets in. e) Melt accumulates at the bottom of the process zone and is pushed forward by the process zone. f, g, h) Melt flows back into the previously formed kerf and closes it.

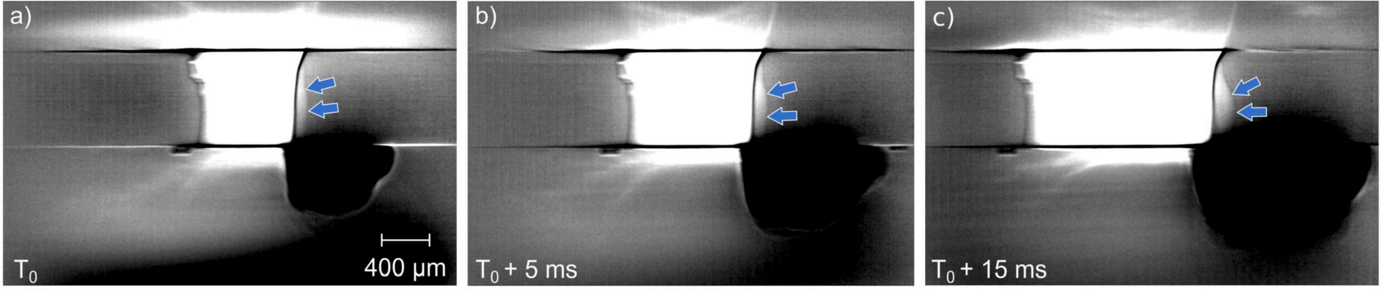

Fig. 14. Enlarged molten area at the cutting front due to the effect of accumulated melt at the bottom of the metal sheet resulting in heat accumulation for $\upsilon_{feed} = 50\,\mathrm{mm\,s^{-1}}$, $P_{laser} = 4\,\mathrm{kW}$.

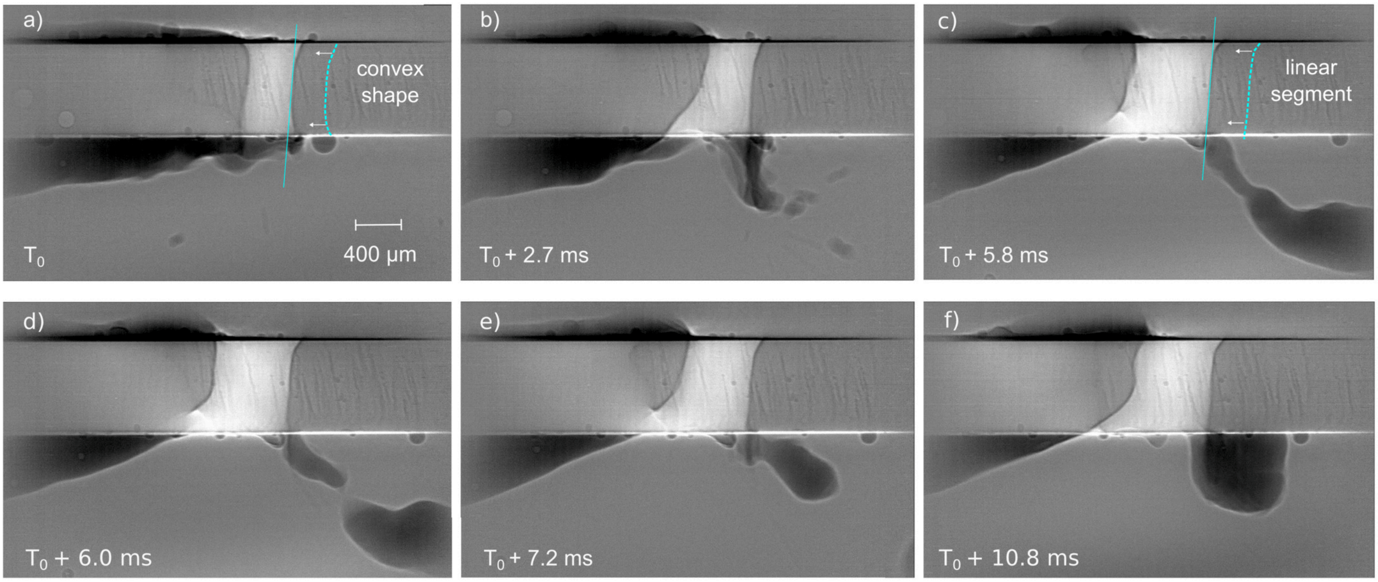

Fig. 15. Transition from a state without melt ejection, to a short period with melt ejection and back for $\upsilon_{feed} = 70\,\mathrm{mm\,s^{-1}}$, $P_{laser} = 4\,\mathrm{kW}$. a) Full penetration welding. The front wall of the keyhole is formed slightly convex, with a strong fluctuation of melt. b) A melt ejection below the front wall. The front wall is straighter in states of melt ejection, pointing to an altered pressure distribution. c) A short period of melt ejection follows, the ejection angle is large. d) A melt drop detaches. e, f) The remaining melt attaches to the bottom of the sample and no further melt ejection occurs.

first resembles a detaching melt stream (c) but moves up and adheres to the bottom of the sample where it accumulates (d, e). As the process zone advances to the region with adhering bulk melt, it pushes it further ahead, but a continuous flow of detaching melt still does not occur (e). This means the first 2 mm of the cut emerge by melt being moved forward out of the process zone, without detachment of the melt from the sample. At some point, the pre-advancement of the accumulated melt in front of the process zone comes to an end (f). The melt flows back into the previously formed cutting kerf and closes part of it (g, h). Shortly after this defect a detaching melt stream emerges and a regular cut is formed. When comparing the video segments of stable RFC with melt detachment to those without melt detachment, no changes in the inclination angle or overall shape of the cutting front are apparent.

3.4.2. *Enlarged melt film at the front wall*

For $P_{laser} = 4\,\mathrm{kW}$, $\upsilon_{feed} = 50\,\mathrm{mm\,s^{-1}}$ (high laser power and low feed velocity) it is observed, that accumulated melt at the bottom of the sample can lead to a enlarged melt film at the cutting front (Fig. 14). The slim sample geometry for the X-ray experiments could enhance this effect, as heat dissipation is limited.

It is not evident from the recordings whether the enlarged molten area has an additional destabilizing effect on the melt ejection, as the enlarged molten area builds due to the already present instable state with accumulated melt at the bottom of the process zone.

3.4.3. *Dynamics at low feed velocities*

For the investigated low feed velocities ($\upsilon_{feed} = 50\,\mathrm{mm\,s^{-1}}$ and $70\,\mathrm{mm\,s^{-1}}$) during most of the processing time, the state resembles Fig. 15 a and no cut is formed. There is a vapour capillary with a diameter similar to the spot diameter and melt flowing around it. For the example in Fig. 15 at $\upsilon_{feed} = 70\,\mathrm{mm\,s^{-1}}$, $P_{laser} = 4\,\mathrm{kW}$, short phases of melt ejection at the bottom of the metal sample occur. This starts with a tilt of the capillary back wall (b) and melt being pushed out directed downwards. While the front wall is fluctuating and slightly convex for the full penetration welding state, likely due to surface tension forces, the front wall gets straighter for the state with melt expulsion. The straight front is possibly caused by altered pressure conditions which also drive the melt ejection. The tilted back wall could be caused by the vapour streaming from the capillary front or by the lack of back streaming melt. Compared to stable RFC at higher feed velocities, the melt ejection is orientated strongly against feed direction (c). After the jet breakup of the melt ejection (d), the part of the jet still connected to the process zone reforms. This occurs due to changes in surface tension forces and adhesive forces once the segment is detached. The melt adheres to the bottom of the metal sheet in front

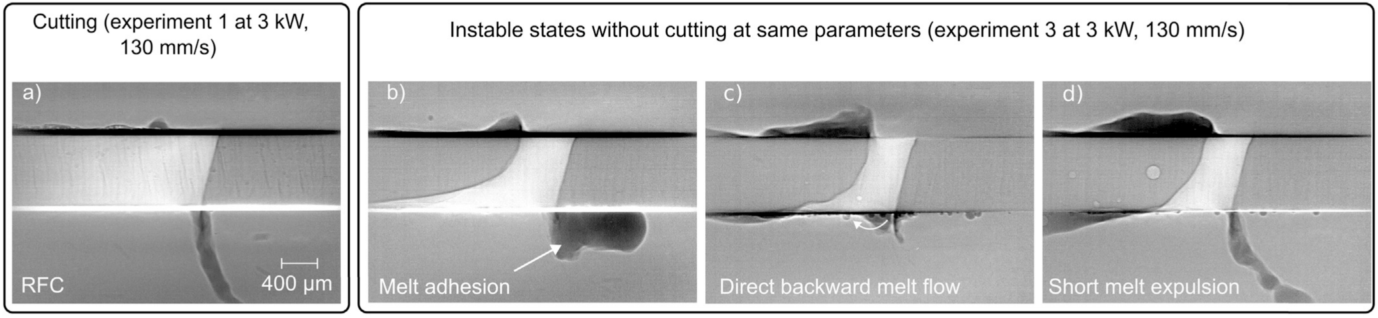

Fig. 16. Observed stable state of RFC in one experiment and instable process zone without cutting for the same parameters of $v_{feed} = 130\,\mathrm{mm\,s^{-1}}$, $P_{laser} = 3\,\mathrm{kW}$.

of the process zone (e). Over the time more melt accumulates there and flows along the bottom of the metal sheet, around the process zone back towards the meltpool (f). During this whole transition the inclination angle of the capillary front remains largely constant. The mechanism responsible for the transition between states of melt ejection and no melt ejection does not appear to be visible in the X-ray videos from this angle of view, given the current temporal and spatial resolution.

3.4.4. Transitional state between keyhole welding and RFC

In the three experiments at $v_{feed} = 130\,\mathrm{mm\,s^{-1}}$, $P_{laser} = 3\,\mathrm{kW}$ it can be observed, that for the same parameters RFC can occur or not. While for one experiment cutting is observed (Fig. 16 a) In one experiment no cutting is observed. The process zone in this experiment without RFC changes between three different states, shown in Fig. 16 b-d: a melt adhesion at the bottom of the sample, a direct backward melt flow at the bottom of the sample and a short period of melt expulsion, which does not last long enough to create a cut. For two experiments RFC evolves after a start with melt accumulation and a short period of full penetration welding. The front wall angles in the experiments are very similar, as shown in Fig. 10 where the three bars are in the same spot at about 74 degree.

In the videos of the two experiments with periods of RFC, there are no changes or only slight changes of about 2 degrees of the inclination angle during the transition from full penetration welding to cutting.

The observation of constant front wall angles for RFC and no RFC indicate, that the changes leading to a melt ejection are either present at a non-visible part of the 3d morphology of the front wall or occur on a very small spatial or temporal scale. One example could be small and fast moving humps at the front wall which are not resolved in the recordings. The melt ejection seems not to be induced by an altered energy deposition due to the *overall* front wall inclination. As pointed out in [7] the *precise* morphology of the front wall plays a crucial role in local absorption and appears to determine the dynamics of the melt at the front wall. Small humps at the front wall alter the local angle of incidence.

3.5. Melt dynamics at the cutting front during processing of AlMg3

The anticipated moving melt humps at the cutting front are not visible in the X-ray recordings for DC04 steel, due to the high velocity and the small size of the structures in combination with the restriction of the framerate by the high density of steel. As it was expected that framerates high enough for such observations in steel might not be reached, the lower density material AlMg3 was imaged for comparison. For AlMg3 a thicker melt film is present at the cutting front. Typical dynamics are shown in Fig. 17. Moving melt humps are present at the cutting front. They form at the top of the sample, and move downwards (a-d). In the middle of the sample the melt humps tend to deform explosively (e). This may be attributed to the time of interaction with the laser beam when the melt hump is travelling downwards and the high absorption of the laser radiation due to the angle of incidence at the surface of the melt bulge. This might be accompanied by the sudden boiling and evaporation of magnesium. High dynamics due to evaporation of magnesium are known from keyhole welding [28]. The explosions cause melt bulges travelling both upward and downward from the center of the explosion (e, f), which lead to spatter detachment. From the upward travelling melt bulge which reaches the top of the sample, the next downward travelling hump emerges and the cycle starts again. For the depicted experiment in Fig. 17 such a cycle takes about 0.2 ms to 0.4 ms.

The first part of the cycle displays similar dynamics as postulated for RFC in [7]: The formation of a hump at the surface of the melt film and its downward movement. The explosions at the humps, after descending partway down the front wall, indicate that energy coupling is high at the hump surfaces, due to their inclination angle. This observation supports the hypothesis of humps at the front wall driving the downward melt movement from [7]. The repeated upward movement of melt does not contribute to a downward-directed melt ejection as observed in RFC of steel. This may be caused by the large amount of molten metal at the front wall together with its low viscosity and high surface tension. Such cyclic melt movements could be suppressed, enhanced or modulated by dynamic energy input at suitable frequencies. This approach may allow for controlling melt ejection and improving the cutting result.

4. Conclusions

This study aimed to generate insights into the process zone during RFC. By utilizing high-speed X-ray imaging, the following results were obtained.

- X-ray imaging of the process zone could be conducted at frame rates up to 18 kHz for DC04 steel and up to 28 kHz for exemplary AlMg3 samples.
- The steel samples display a process zone with a thin melt film at the cutting front and a melt flow from the process zone directed against feed direction. In contrast, the AlMg3 samples display a ticker melt film at the cutting front. For AlMg3, there is no continuous melt flow out of the process zone; instead spatter detaches in feed direction.
- In RFC there is no rear wall of the process zone like in keyhole welding, reducing energy input by multiple reflections of the laser radiation. Despite this difference, the inclination angle of the cutting front aligns with the theoretical curve for keyhole welding from [13].
- The position of melt ejection for low feed velocities is located at the bottom foremost point of the cutting front. For high feed velocities the side walls of the process zone contribute to the melt ejection. For high feed velocities a melt ejection to the surface of the samples is present.

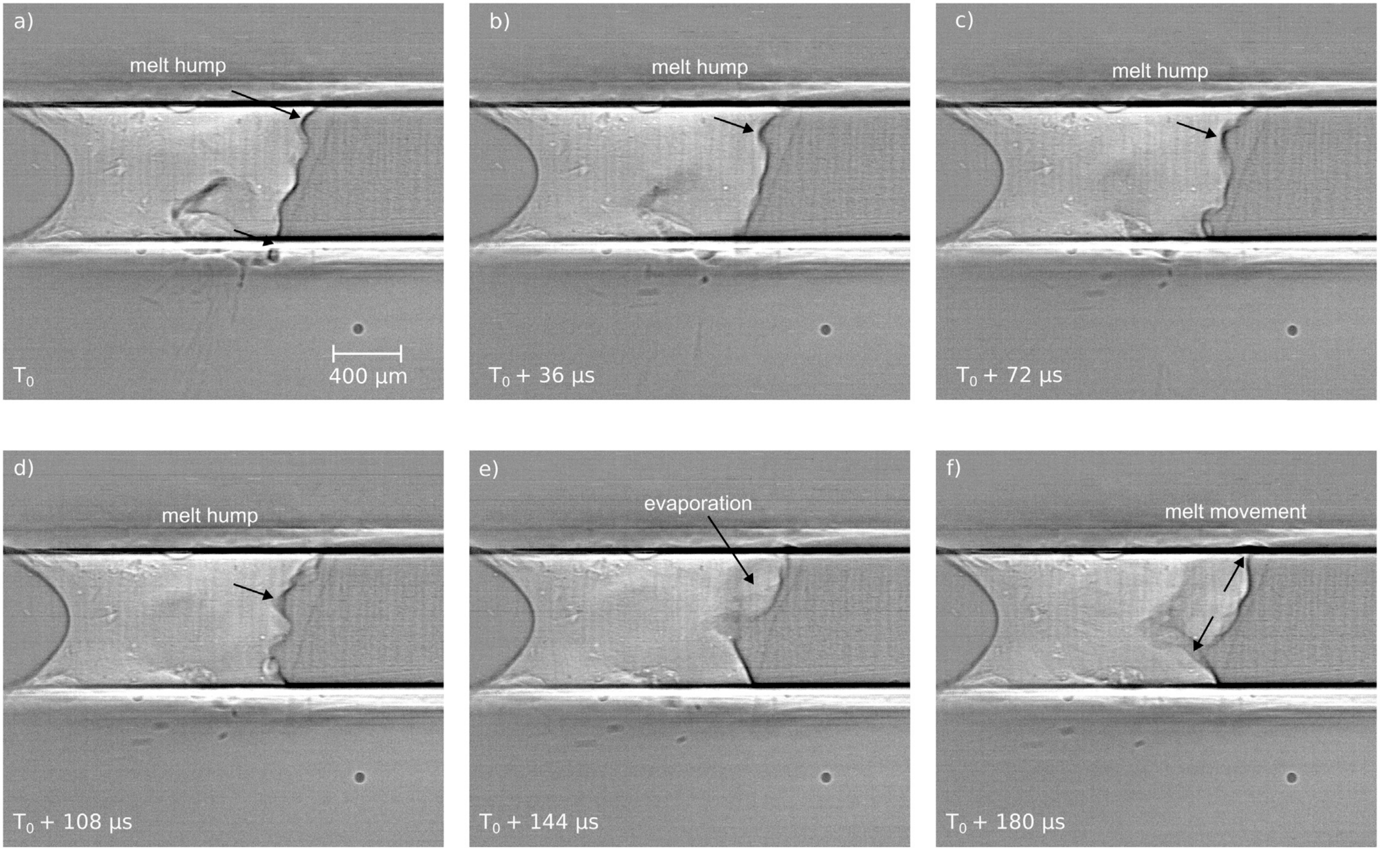

Fig. 17. Melt dynamics at the cutting front for AlMg3 $v_{feed} = 190\,\mathrm{mm\,s^{-1}}$, $P_{laser} = 3\,\mathrm{kW}$ at a framerate of 28 kHz. Moving melt humps are observed. A cyclic pattern evolves: a melt bulge forms at the top of the process zone (a, b) and moves downward (c, d). In the middle of the process zone, the melt bulge suddenly evaporates and pushes melt away from the evaporation center, upwards and downwards. At the top a new melt bulge forms and the cycle is repeated. The cycle displayed here has a duration of about 180 µs.

- With refraction enhanced imaging the melt film thickness at the front wall can be determined, which was measured in the range from 40 µm to 80 µm. For high feed velocities, the thickness is even lower and could not be clearly resolved. The melt film thickness decreases with increasing feed velocity.
- Exemplary transitions from full penetration welding to RFC display no change in the cutting front inclination. Only for low feed velocities a change in the form of the frontwall was observed. This suggests that the front wall inclination is not the factor determining if a melt ejection and a state of cutting is present. The changes leading to a melt ejection are either present at a non-visible part of the 3d morphology of the front wall or occur on a very small spatial or temporal scale. One example are the small and fast moving humps at the front wall which are not resolved in the recordings.
- The detailed cutting front topography with small melt humps could not be resolved at the temporal and spatial resolution of the recordings for the DC04 samples. This was achieved at higher framerates for AlMg3. There, the melt film at the cutting front displays temporally cyclic patterns of movement. The downward movement of the melt in the beginning and the explosions at the shoulders of the downward travelling humps confirm that the humps play an important role in the process dynamics.

In sum, high-speed X-ray imaging reveals typical characteristics of the process zone like the cutting front profile and inclination angle, together with the melt ejection direction. Future investigations of RFC by X-ray imaging should aim for even higher flux, to enable even higher temporal resolution. Furthermore, tracer particles could help analyzing the melt flow in the process zone. The mechanisms in the melt film at the cutting front should be analyzed, as well as the flow on the sidewalls of the process zone, which leads to the melt ejection at the top of the metal sample. The cyclic behaviour of the melt at the front wall of the AlMg3 samples should be further investigated regarding parameter dependence and periodicity. It might be possible to influence the dynamics by temporal modulation of the laser beam intensity to obtain a steady melt expulsion.

CRediT authorship contribution statement

Silvana Burger: Writing – review & editing, Writing – original draft, Visualization, Validation, Software, Methodology, Investigation, Formal analysis, Data curation, Conceptualization. **Carola Forster:** Writing – review & editing, Investigation. **Christoph Spurk:** Investigation. **Marc Hummel:** Investigation. **Alexander Olowinsky:** Funding acquisition. **Felix Beckmann:** Investigation. **Julian Moosmann:** Investigation. **Michael Schmidt:** Supervision, Project administration, Funding acquisition, Conceptualization.

Declaration of competing interest

The authors declare that they have no known competing financial interests or personal relationships that could have appeared to influence the work reported in this paper.

Acknowledgements

This work was funded by the Deutsche Forschungsgemeinschaft (DFG, German Research Foundation) – 407703212.

The presented investigations were carried out within the cooperation “Laser Meets Synchrotron” (www.laser-meetssynchrotron.de). The experimental setup and its operation were funded by the Deutsche Forschungsgemeinschaft e.V. (DFG, German Research Foundation) within the framework of the Collaborative Research Centre SFB1120-236616214 “Bauteilpräzision durch Beherrschung von Schmelze und Erstarrung in Produktionsprozessen”. The experiments were carried out in cooperation with Helmholtz-Zentrum Hereon in Hamburg at DESY PETRA III and we would like to thank all people involved for their support.

The authors gratefully acknowledge funding of the Erlangen Graduate School in Advanced Optical Technologies (SAOT) by the Bavarian State Ministry for Science and Art.

Data availability

Data will be made available on request.

References

[1] Riveiro A, Quintero F, Boutinguiza M, Del Val J, Comesaña R, Lusquiños F, et al. Laser cutting: a review on the influence of assist gas. Materials 2019;12(1):157. https://doi.org/10.3390/ma12010157. https://www.mdpi.com/1996-1944/12/1/157.

[2] Schäfer P. Schneiden auf abstand. ATZproduktion 2010;3(2):24–8. https://doi.org/10.1007/BF03224129. https://link.springer.com/article/10.1007/BF03224129.

[3] Wagner A, Lütke M, Wetzig A, Eng LM. Laser remote-fusion cutting with solid-state lasers. J Laser Appl 2013;25(5). https://doi.org/10.2351/1.4816651. https://pubs.aip.org/lia/jla/article/25/5/052004/221377/Laser-remote-fusion-cutting-with-solid-state.

[4] Zaeh MF, Moesl J, Musiol J, Oefele F. Material processing with remote technology revolution or evolution? Phys Proc 2010;5:19–33. https://doi.org/10.1016/j.phpro.2010.08.119. https://www.sciencedirect.com/science/article/pii/S1875389210005456.

[5] Villumsen S, Kristiansen M. Angular stability margins for the remote fusion cutting process. Phys Proc 2015;78:89–98. https://doi.org/10.1016/j.phpro.2015.11.021. https://www.sciencedirect.com/science/article/pii/S1875389215015114.

[6] Schober A, Musiol J, Daub R, Feil J, Zaeh MF. Experimental investigation of the cutting front angle during remote fusion cutting. Phys Proc 2012;39:204–12. https://doi.org/10.1016/j.phpro.2012.10.031. https://www.sciencedirect.com/science/article/pii/S1875389212025588.

[7] Kaplan AF. Local flashing events at the keyhole front in laser welding. Opt Lasers Eng 2015;68:35–41. https://doi.org/10.1016/j.optlaseng.2014.12.019.

[8] Kaplan AFH, Matti RS. Absorption peaks depending on topology of the keyhole front and wavelength. J Laser Appl 2015;27(S2). https://doi.org/10.2351/1.4906469.

[9] Zhang C, Wen P, Yao Z, Yuan Y, Fan X. Visualization of flow separation inside cut kerf during laser cutting of thick sections. J Laser Appl 2016;28(2):022204. https://doi.org/10.2351/1.4943997. https://lia.scitation.org/doi/10.2351/1.4943997.

[10] Arntz-Schroeder D, Petring D. Analyzing the dynamics of the laser beam cutting process. PhotonicsViews 2020;17(2):43–7. https://doi.org/10.1002/phvs.202000015. https://onlinelibrary.wiley.com/doi/pdf/10.1002/phvs.202000015.

[11] Sawannia M, Borkmann M, Herwig P, Wetzig A, Weber R, Graf T. Influence of laser beam oscillation on the cutting front geometry investigated by high-speed 3d-measurements. Proc CIRP 2022;111:736–9. https://doi.org/10.1016/j.procir.2022.08.100. https://www.sciencedirect.com/science/article/pii/S2212827122009817.

[12] Stoyanov S, Petring D, Arntz-Schroeder D, Günder M, Gillner A, Poprawe R. Investigation on the melt ejection and Burr formation during laser fusion cutting of stainless steel. J Laser Appl 2020;32(2). https://doi.org/10.2351/7.0000074.

[13] Fabbro R. Melt pool and keyhole behaviour analysis for deep penetration laser welding. J Phys D, Appl Phys 2010;43(44):445501. https://doi.org/10.1088/0022-3727/43/44/445501.

[14] Cunningham R, Zhao C, Parab N, Kantzos C, Pauza J, Fezzaa K, et al. Keyhole threshold and morphology in laser melting revealed by ultrahigh-speed x-ray imaging. Science (New York, NY) 2019;363(6429):849–52. https://doi.org/10.1126/science.aav4687.

[15] Mayi YA, Dal M, Peyre P, Bellet M, Fabbro R. Physical mechanisms of conduction-to-keyhole transition in laser welding and additive manufacturing processes. Opt Laser Technol 2023;158:108811. https://doi.org/10.1016/j.optlastec.2022.108811. https://www.sciencedirect.com/science/article/pii/S0030399222009574.

[16] Fabbro R. Depth dependence and keyhole stability at threshold, for different laser welding regimes. Appl Sci 2020;10(4):1487. https://doi.org/10.3390/app10041487. https://www.mdpi.com/2076-3417/10/4/1487.

[17] Paleocrassas AG, Tu JF. Inherent instability investigation for low speed laser welding of aluminum using a single-mode fiber laser. J Mater Process Technol 2010;210(10):1411–8. https://doi.org/10.1016/j.jmatprotec.2010.04.002. https://www.sciencedirect.com/science/article/pii/S0924013610001123.

[18] Burger S, Dilger P, Eschner E, Schmidt M. Quantification of melt dynamics from high-speed observations within the remote fusion cutting regime by means of image processing. In: Behrens B-A, Brosius A, Drossel W-G, Hintze W, Ihlenfeldt S, Nyhuis P, editors. Production at the leading edge of technology, lecture notes in production engineering. Cham: Springer International Publishing and Imprint Springer; 2022. p. 328–36.

[19] Hagenlocher C, Lind J, Weber R, Graf T. High-speed x-ray investigation of pore formation during full penetration laser beam welding of aa6016 aluminum sheets contaminated with lubricants. Appl Sci 2020;10(6):2077. https://doi.org/10.3390/app10062077. https://www.mdpi.com/2076-3417/10/6/2077.

[20] Willmott P. An introduction to synchrotron radiation: techniques and applications. second edition. Hoboken, NJ: John Wiley & Sons Inc; 2019. https://onlinelibrary.wiley.com/doi/book/10.1002/9781119280453.

[21] Lind J, Hagenlocher C, Blazquez-Sanchez D, Hummel M, Olowinsky A, Weber R, et al. Influence of the laser cutting front geometry on the striation formation analysed with high-speed synchrotron x-ray imaging. IOP Conf Ser, Mater Sci Eng 2021;1135(1):012009. https://doi.org/10.1088/1757-899X/1135/1/012009. https://iopscience.iop.org/article/10.1088/1757-899X/1135/1/012009.

[22] Hollatz S, Hummel M, Olowinsky A, Gillner A, Beckmann F, Moosmann J. Pore formation and melt pool analysis of laser welded al-cu joints using synchrotron radiation. J Mater Process Technol 2022;309:117738. https://doi.org/10.1016/j.jmatprotec.2022.117738. https://www.sciencedirect.com/science/article/pii/S0924013622002497.

[23] Chen Y, Clark SJ, Leung CLA, Sinclair L, Marussi S, Olbinado MP, et al. In-situ synchrotron imaging of keyhole mode multi-layer laser powder bed fusion additive manufacturing. Appl Mater Today 2020;20:100650. https://doi.org/10.1016/j.apmt.2020.100650. https://www.sciencedirect.com/science/article/pii/S2352940720300986.

[24] van der Walt S, Schönberger JL, Nunez-Iglesias J, Boulogne F, Warner JD, Yager N, et al. scikit-image: image processing in python. PeerJ 2014;2:e453. https://doi.org/10.7717/peerj.453.

[25] Savitzky A, Golay MJE. Smoothing and differentiation of data by simplified least squares procedures. Anal Chem 1964;36(8):1627–39. https://doi.org/10.1021/ac60214a047.

[26] Jordan DTA, Ribe NM, Deblais A, Bonn D. Chain oscillations in liquid jets. Phys Rev Fluids 2022;7(10):104001. https://doi.org/10.1103/PhysRevFluids.7.104001.

[27] Sanjay V, Das AK. Formation of liquid chain by collision of two laminar jets. Phys Fluids 2017;29(11). https://doi.org/10.1063/1.4998288. https://pubs.aip.org/aip/pof/article/29/11/112101/105478/Formation-of-liquid-chain-by-collision-of-two.

[28] Zhou L, Zhang M, Jin X, Zhang H, Mao C. Study on the burning loss of magnesium in fiber laser welding of an al-mg alloy by optical emission spectroscopy. Int J Adv Manuf Technol 2017;88(5–8):1373–81. https://doi.org/10.1007/s00170-016-8867-y. https://link.springer.com/article/10.1007/s00170-016-8867-y.